The Astrophysical Journal, 930:100 (14pp), 2022 May 10 https://doi.org/10.3847/1538-4357/ac62ce

A Study of Photoionized Gas in Two H II Regions of the N44 Complex in the LMC Using MUSE Observations

Susmita Barman[1,2], Naslim Neelamkodan[1], Suzanne C. Madden[3], Marta Sewilo[4,5], Francisca Kemper[6,7], Kazuki Tokuda[8,9,10], Soma Sanyal[2], and Toshikazu Onishi[8]
[1] Department of Physics, College of Science, United Arab Emirates University (UAEU), Al-Ain, 15551, UAE; naslim.n@uaeu.ac.ae
[2] School of Physics, University of Hyderabad, Prof. C. R. Rao Road, Gachibowli, Telangana, Hyderabad, 500046, India
[3] Laboratoire AIM, CEA/DSM - CEA Saclay, F-91191 Gif-sur-Yvette, France
[4] CRESST II and Exoplanets and Stellar Astrophysics Laboratory, NASA Goddard Space Flight Center, Greenbelt, MD 20771, USA
[5] Department of Astronomy, University of Maryland, College Park, MD 20742, USA
[6] European Southern Observatory, Karl-Schwarzschild-Str. 2, D-85748, Garching b. München, Germany
[7] Institute of Astronomy and Astrophysics, Academia Sinica, 11F of Astronomy-Mathematics Building, AS/NTU, No.1, Sec. 4, Roosevelt Rd., Taipei 10617, Taiwan
[8] Department of Physical Science, Graduate School of Science, Osaka Prefecture University, 1-1 Gakuen-cho, Sakai, Osaka 599-8531, Japan
[9] Department of Physics, Graduate School of Science, Osaka Metropolitan University, 1-1 Gakuen-cho, Naka-ku, Sakai, Osaka 599-8531, Japan
[10] Department of Earth and Planetary Sciences, Faculty of Sciences, Kyushu University, Nishi-ku, Fukuoka 819-0395, Japan
Received 2021 July 25; revised 2022 March 24; accepted 2022 March 29; published 2022 May 9

Abstract

We use the optical integral field observations with Multi-Unit Spectroscopic Explorer (MUSE) on the Very Large Telescope, together with CLOUDY photoionization models, to study ionization structure and physical conditions of two luminous H II regions in the N44 star-forming complex of the Large Magellanic Cloud. The spectral maps of various emission lines reveal a stratified ionization geometry in N44 D1. The spatial distribution of [O I] λ6300 emission in N44 D1 indicates a partially covered ionization front at the outer boundary of the H II region. These observations reveal that N44 D1 is a blister H II region. The [O I] λ6300 emission in N44 C does not provide a well-defined ionization front at the boundary, while patches of [S II] λ6717 and [O I] λ6300 emission bars are found in the interior. The results of spatially resolved MUSE spectra are tested with the photoionization models for the first time in these H II regions. A spherically symmetric ionization-bounded model with a partial covering factor, which is appropriate for a blister H II region, can well reproduce the observed geometry and most of the diagnostic line ratios in N44 D1. Similarly, in N44 C we apply a low-density and optically thin model based on the observational signatures. Our modeling results show that the ionization structure and physical conditions of N44 D1 are mainly determined by the radiation from an O5 V star. However, local X-rays, possibly from supernovae or stellar wind, play a key role. In N44 C, the main contribution is from three ionizing stars.

Unified Astronomy Thesaurus concepts: H II regions (694); Large Magellanic Cloud (903); Photoionization (2060); Interstellar line emission (844)

1. Introduction

Massive stars are the significant sources of ultraviolet (UV) radiation in galaxies with energies high enough (>13.6 eV) to ionize the neutral gas in the interstellar medium (ISM). A part of this high-energy radiation is absorbed by the neutral gas and heats the surrounding medium, creating the ionized H II regions. A large fraction of this ionizing radiation escapes into the diffuse medium, penetrating the molecular gas, if some part of the H II region is optically thin. This creates an ionization zone (H^+), an ionization front (H^0), and a photodissociation region (PDR). The ionization front is at the outer boundary of an H II region that lies inside the PDR. There have been several studies of Galactic and extragalactic H II regions and PDRs, e.g., Orion Nebula (Pogge et al. 1992; García-Díaz & Henney 2007), 30 Doradus (Pellegrini et al. 2010), NGC 364 (Peimbert et al. 2000; Relano et al. 2002), dense H II regions in IC 10 (Polles et al. 2019), and NGC 595 (Relaño et al. 2010). The impact of ionizing radiation on the surrounding medium and the physical properties of H II regions are normally obtained by strong emission lines in the optical spectrum, which is mainly populated by hydrogen recombination lines and forbidden lines of other common elements. These gas emission lines are sensitive to physical conditions such as density and temperature; hence, their relative intensities can probe the physical mechanism involved in the ionization processes.

The Large Magellanic Cloud (LMC) is an ideal laboratory to study the properties of H II regions and the massive star feedback in a low-metallicity galaxy owing to its subsolar metallicity ($Z = 0.5\ Z_{\odot}$; Westerlund 1997), face-on viewing angle (van der Marel & Cioni 2001), reduced extinction along the line of sight, and a distance of 50 kpc (Pietrzyński et al. 2019), allowing the spatially resolved observations of the ISM structures on subparsec scales. Naslim et al. (2015) have reported on 10 PDRs in the LMC using H_2 pure rotational transition emission obtained with Spitzer. These regions include intense H II regions, diffuse ISM clouds, and dense molecular clouds. We study the individual clouds in detail using various observations to investigate the high-mass star formation (see Naslim et al. 2018; Nayana et al. 2020) and its impact on the ISM. To explore the impact of ionizing radiation from massive stars on the surrounding medium, we revisit two H II regions in a well-studied star-forming complex of the LMC, N44. We examine the physical conditions and ionization structure of N44D and N44C by comparing the observations

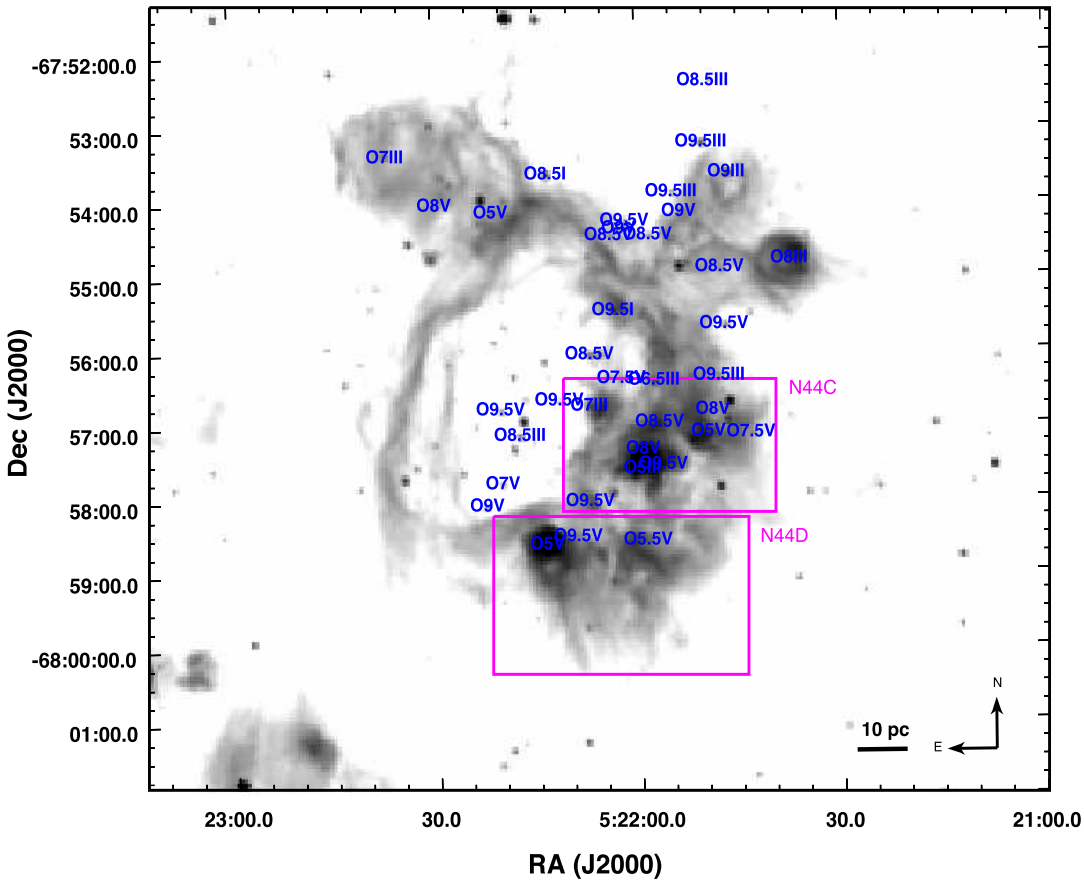

Figure 1. The Hα map of the whole N44 superbubble obtained from the Magellanic Cloud Emission Line Survey (MCELS; Smith & MCELS Team 1998). Spectral types of hot stars (McLeod et al. 2019) are labeled on the Hα emission map, and the magenta boxes indicate the N44 D and N44 C H II regions.

with the predictions of the photoionization model, CLOUDY (Ferland et al. 2017).

The N44 superbubble is one of the brightest star-forming regions in the LMC, which can be clearly traced by its compact H II regions along the main shell rim in an Hα map (Figure 1). The region is powered by nearly 35−38 hot stars (Oey & Massey 1995; McLeod et al. 2019) of stellar associations LH47, LH48, and LH49 (Lucke & Hodge 1970). McLeod et al. (2019) report the analysis of radiative and mechanical feedback from massive stars in the H II regions of N44 (N44 A, N44 B, N44 C, and N44 D) using the optical integral field data from Multi-Unit Spectroscopic Explorer (MUSE). They used the He II λ5412 line to identify the feedback driving massive stars, and they estimated the spectral types and luminosity classes of these stars for determining the stellar radiative output. Using the nebular emission-line maps of Hα, Hβ, [S II] $\lambda\lambda$6717, 6732, [N II] λ6584, and [O III] λ5007, they derived the electron density from the [S II] $\lambda6717/\lambda6732$ ratio assuming a nebular electron temperature of 10,000 K. They also derived the degree of ionization using the [O II]/[O III] ratio, kinematics, and the oxygen abundances. In addition, they explored the role of different stellar feedback mechanisms by estimating various pressures and found that the H II region expansion is mainly driven by stellar radiation pressure and ionized gas.

In this paper, we further explore the rich nebular emission lines in the MUSE data set (McLeod et al. 2019) of N44 for a detailed understanding of their spatial distributions, ionization structures, and physical conditions. We compare these results with the photoionization models to interpret the observations of this star-forming complex. The MUSE archival data of N44 provide many iconic emission lines, such as Hα, Hβ, [S III] λ9069, [S II] $\lambda\lambda$6717, 6732, [O III] $\lambda\lambda$4959, 5007, [O II] $\lambda\lambda$7318, 7329, [O I] λ6300, and [N II] λ6584, that have only been partially utilized in McLeod et al. (2019). We exploit various emission-line ratios to study the behavior of different ionization zones and compare the observed line ratios with the best-fit photoionization models to further understand the physical process.

The N44 main shell is surrounded by several Hα bright regions (Figure 1). The compact H II region on the southwest rim of the shell, N44 D, is the most luminous one in N44 (McLeod et al. 2019). We choose the two brightest H II regions N44 D and N44 C for our study, which show higher degree of ionization than N44 A and N44 B, and nearly spherical ionization structures with different feedback characteristics based on studies by McLeod et al. (2019). N44 D encloses three hot stars of spectral type O5 V, O9.5 V, and O5.5 V (McLeod et al. 2019). The second-brightest H II region, N44 C, is adjacent to N44D on the western rim of the shell, and the region harbors three hot stars of spectral type O5 III, O9.5 V, and O5 III (McLeod et al. 2019). One reason for selecting N44 D is that MUSE observations show an edge-on ionization front, allowing a detailed study of ionization as a function of depth into the cloud. At first glance, N44 C does not show such

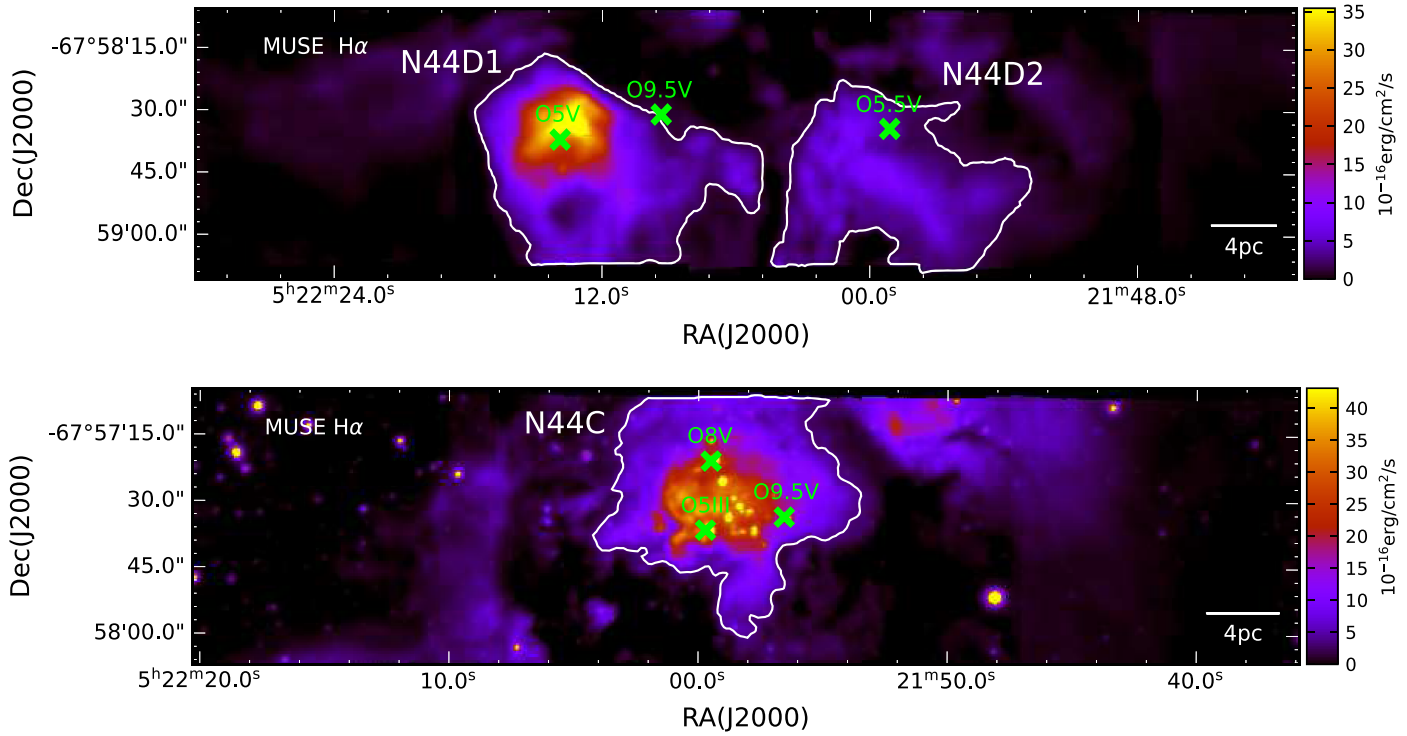

Figure 2. The MUSE Hα maps of N44 D (top) and N44 C (bottom). The emission-line fluxes are extracted from the polygon regions (white) of N44 D1, N44 D2, and N44 C for the analysis of photoionized gas in this work.

a well-defined ionization front at the H II region boundary, while it shows a higher photon escape fraction relative to N44 D than reported by McLeod et al. (2019). These two nebulae show different ionization structures; hence, physical processes of two different types of H II regions can be compared. Moreover, the hot star contents of N44 H II regions are extensively studied, and high spatial resolution observations are readily available. This study allows us to directly apply the observed stellar parameters, gas densities, and emission-line intensities to constrain the photoionization model without arbitrary assumption, as well as to test their influence on the geometry of the H II regions.

2. Observations

We used the MUSE archival data of N44 C and N44 D (program ID: 096.C-0137(A); PI: A. F. McLeod). MUSE is a large field-of-view (FOV) integral field unit (IFU) panchromatic optical instrument on the European Southern Observatory's (ESO) Very Large Telescope (VLT) in Paranal, Chile. This instrument provides high spatial resolution observations at a pixel scale of 0.2″, with a resolving power ranging from 1770 to 3590. The observations of N44 C and N44 D have been taken on 2015 October 21 and 2016 February 25, with the MUSE_wfm-noao_obs_genericoffset observing template, in a wide-field observing mode covering a wavelength range 475−935 nm. The reduced MUSE data are retrieved from the ESO science archive.[11] The data were reduced using the MUSE-1.6.1 pipeline. The MUSE pipeline process automatically removes most of the instrumental signatures. The raw data were preprocessed, and bias subtraction, flat-fielding, sky-subtraction, wavelength calibration, and flux calibration were applied. These data were not taken with the Adaptive Optics System of MUSE, and the seeing-limited angular resolutions 0.98″ and 1.30″ are achieved for N44 D and N44 C, respectively. We note that no point-spread function (PSF) matching was applied for subsequent analysis, and all the analyzed regions are resolved regardless of the achieved seeing. Our analysis is based on integrated line flux maps; hence, no PSF information is retained.

[11] http://archive.eso.org/cms.html

3. Emission-line Maps of N44 D and N44 C

Figure 2 shows the extinction-corrected Hα line flux maps of N44 D and N44 C obtained with MUSE. The ionized gas traced by the Hα emission shows two H II regions in N44 D, those we label as N44 D1 and N44 D2, and one in N44 C. Even though the regions are nearly spherical, their boundaries cannot be directly specified in a circular aperture. Hence, for determining the boundaries of these Hα-bright regions based on their surface brightness, we use the Python package ASTRODENDRO (Rosolowsky et al. 2008). This algorithm identifies and characterizes the hierarchical structures in the emission-line map as a structure tree, where each entity is represented as an isosurface. The local maxima represent the top level of the dendrogram and are identified from the emission-line map with the flux $>3\sigma$. The isosurfaces (two-dimensional contours) that surround the local maxima are leaves, branches, and trunks. The trunks represent parent structures that enclose the branches connecting two leaves. Further description and methods of using ASTRODENDRO can be found in Naslim et al. (2018). Della Bruna et al. (2020) have recently used ASTRODENRO to identify Hα-bright regions in MUSE maps of NGC 7793 by applying a similar method. We define the boundary of H II regions in the Hα map that are identified as trunks with ASTRODENDRO. The lower contour levels of these trunks are taken as the boundaries of H II regions within the chosen

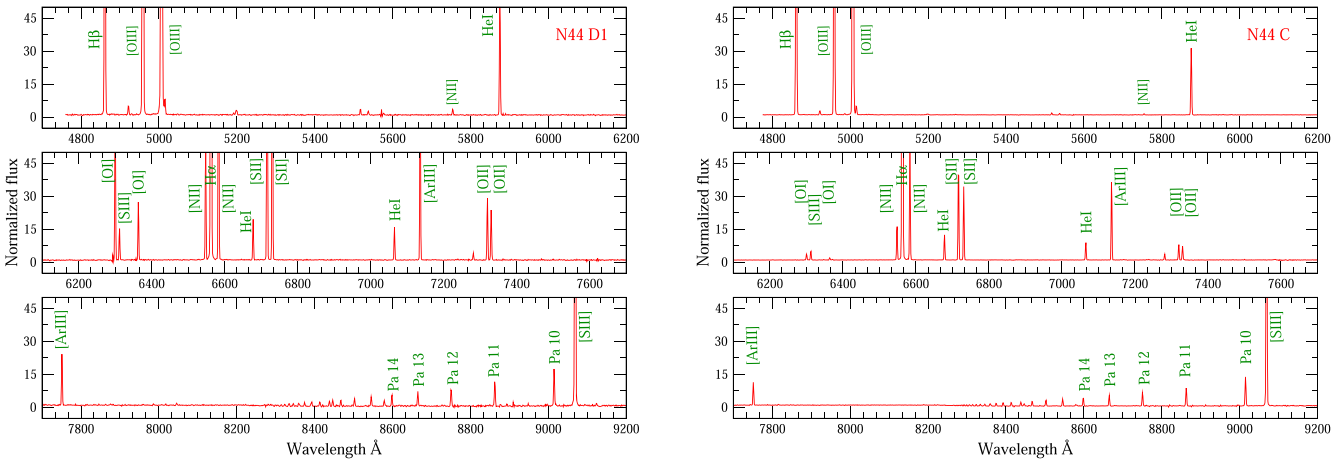

Figure 3. The identified emission lines are labeled in the MUSE spectra extracted from a 1.0″-radius circular region close to the crosscut indicated as a red line in Figure 6. This is to show the rich emission lines available for analysis in the MUSE observation of N44 D1 and N44 C. The continua of the spectra are normalized to 1, and the peaks of certain strong lines are cut out of the scale for the weaker lines to be visible in the plot properly.

observation field. These regions appear as polygons in Figure 2.

In addition to Hα λ6562.8 emission, the MUSE spectra of N44 D1 and N44 C show emission due to Hβ λ4861, [O III] $\lambda\lambda$5007, 4959, [O II] $\lambda\lambda$7318, 7329, [O I] λ6300, [N II] λ6584, [S II] $\lambda\lambda$6717, 6732, [S III] λ9069, [Ar III] $\lambda\lambda$7135, 7751, and many He I and Paschen hydrogen lines (Figure 3). Figure 6 shows integrated line flux maps of Hβ, [S II] λ6717, [O III] λ5007, [O II] λ7318, [O I] λ6300, and [N II] λ6584 in N44 D1, N44 D2, and N44 C. Hβ and [O III] λ5007 emission shows similar spatial distribution to the Hα emission in both N44 D and N44 C, while [S II], [O II], [N II], and [O I] emission in N44 D1 shows a shell structure. The morphology of N44 D2 is irregular with pillars or filamentary structures. The continuum subtraction is applied by creating continuum maps from the user-defined line-free portions of the spectrum around each emission line. The line fluxes (erg s^{-1} cm^{-2}) of N44 D1, N44 D2, and N44 C regions are then extracted from the integrated line flux maps by applying aperture photometry within the specified regions as polygon structures obtained from ASTRODENDRO. Only the pixel values with S/N > 10 are considered within all the polygons. These fluxes are then point-source flux removed by subtracting the point-source fluxes, which are also extracted within the user-defined apertures. For uncertainties, we added in quadrature the error in aperture photometry and an expected 20% calibration error in every line flux measurement. The error in photometry is the quadratically added uncertainty in measurements over all pixels within a region.

To check the data reduction and flux calibration quality of the data cube retrieved from the MUSE archive, we compared the Hα line luminosities (erg s^{-1}) of N44 C and N44 D1 from the MUSE archival data to the Hα luminosities presented in McLeod et al. (2019). In Table 1 we show the comparison of Hα luminosities obtained from the data presented in this work and McLeod et al. (2019). We note that the line luminosities obtained from the two data sets agree within the estimated uncertainties; hence, we are confident to proceed with the analysis of pipeline-reduced MUSE archival data. The observed line luminosities (erg s^{-1}) are given in Table 2. We choose two bright regions, N44 D1 and N44 C, for further analysis with photoionization models.

Table 1
Comparison of Hα Luminosities Obtained from the MUSE Archival Pipeline Data (This Work) with the Data Obtained from McLeod et al. (2019)

N44 D1		N44 C	
[a]L_{obs}(erg s^{-1}) ($\times 10^{37}$)	[b]L_{obs}(erg s^{-1}) ($\times 10^{37}$)	[a]L_{obs}(erg s^{-1}) ($\times 10^{37}$)	[b]L_{obs}(erg s^{-1}) ($\times 10^{37}$)
1.47 ± 0.16	1.47	1.39 ± 0.15	1.51

Notes.
[a] MUSE archival data used in this work.
[b] McLeod et al. (2019).

4. Emission-line Ratios: [S II]/Hα, [N II]/Hα, [O III]/Hα, and [O III]/Hβ

We present the extinction-corrected [S II] λ6717/Hα, [N II] λ6584/Hα, [O III] λ5007/Hα, and [O III] λ5007/Hβ ratio maps of N44 D and N44 C in Figures 4 and 5, respectively. These ratios allow us to study the ionization structure of the region. [S II] λ6717/Hα and [N II] λ6584/Hα are lower at the central regions closer to the ionizing stars, implying a higher ionization zone, while at the periphery the values of these ratios are higher, indicating a low ionization zone. We find that both [S II] λ6717/Hα and [N II] λ6584/Hα maps of N44 D1 and N44 C show a shell morphology. The central part of the N44 D1 has a lower [S II] λ6717/Hα ratio ($\sim$0.02), and at the periphery its value is $\sim$0.3. N44 C shows an [S II] λ6717/Hα value of $\sim$0.04 at the center and a value of $\sim$0.20 at the periphery. Similarly, the value of the [N II] λ6584/Hα ratio ranges from 0.03 to 0.20 in N44 D1 and from 0.04 to 0.15 in N44 C. The model calculations by Allen et al. (2008) have shown that [S II]/Hα and [N II]/Hα ratios greater than 0.39 and 0.79 would be a result of strong contributions from shocks. The [S II]/Hα and [N II]/Hα ratios of both N44 D1 and N44 C are well below the values 0.39 and 0.79, respectively, indicating a substantial contribution from photoionization. However, in the regions outside the boundary of these H II regions, we find the enhanced [S II]/Hα and [N II]/Hα ratios; hence, the contribution from shocks cannot be totally ignored.

A similar effect is found in the [O III] λ5007/Hβ and [O III] λ5007/Hα ratios. The values are higher in the regions

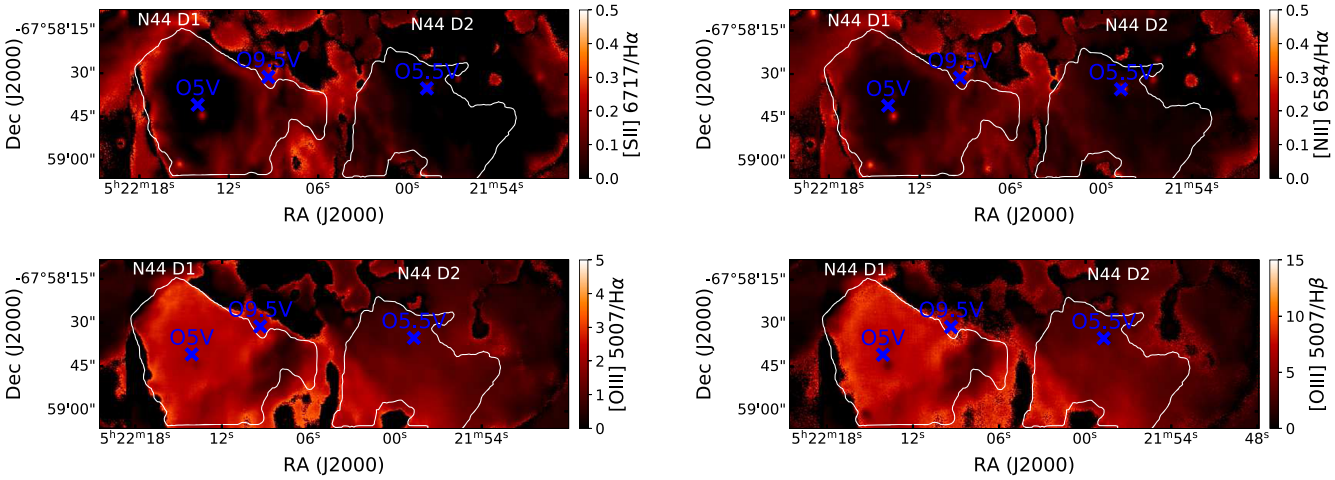

Figure 4. [S II] λ6717/Hα, [N II] λ6584/Hα, [O III] λ5007/Hα, and [O III] λ5007/Hβ ratio maps of N44 D1 and N44 D2 regions. The white polygons represent the regions taken for analysis in this work, and blue crosses are the locations of hot stars.

Table 2
Luminosities of Observed Emission Lines

Emission Lines	N44 D1		N44 D2		N44 C	
	L_{obs}(erg s^{-1})[a] ($\times 10^{36}$)	L_{int}(erg s^{-1})[b] ($\times 10^{36}$)	L_{obs}(erg s^{-1}) ($\times 10^{36}$)	L_{int}(erg s^{-1}) ($\times 10^{36}$)	L_{obs}(erg s^{-1}) ($\times 10^{36}$)	L_{int}(erg s^{-1}) ($\times 10^{36}$)
Hα	14.70 ± 1.62	17.5 ± 1.93	5.36 ± 0.58	5.45 ± 0.69	13.9 ± 1.53	21.5 ± 1.86
Hβ	4.68 ± 0.47	6.12 ± 0.61	1.71 ± 0.24	1.76 ± 0.31	3.69 ± 0.55	7.24 ± 0.75
[N II] λ6584	0.80 ± 0.13	0.96 ± 0.16	0.29 ± 0.07	0.30 ± 0.08	0.97 ± 0.16	1.50 ± 0.20
[O I] λ6300	0.32 ± 0.07	0.39 ± 0.08	0.07 ± 0.03	0.07 ± 0.03	0.13 ± 0.04	0.21 ± 0.05
[O II] λ7318	0.16 ± 0.05	0.19 ± 0.06	0.06 ± 0.03	0.06 ± 0.03	0.17 ± 0.05	0.24 ± 0.06
[O II] λ7329	0.15 ± 0.04	0.17 ± 0.04	0.05 ± 0.02	0.05 ± 0.02	0.14 ± 0.04	0.20 ± 0.04
[O III] λ4959	12.40 ± 0.64	16.1 ± 2.13	2.98 ± 0.38	3.06 ± 0.50	2.61 ± 0.04	5.02 ± 0.56
[O III] λ5007	36.90 ± 3.85	48.5 ± 5.06	8.87 ± 0.99	9.11 ± 1.30	7.66 ± 1.09	15.1 ± 1.48
[S II] λ6717	1.11 ± 0.16	1.31 ± 0.18	0.34 ± 0.07	0.35 ± 0.08	0.94 ± 0.15	1.43 ± 0.18
[S II] λ6732	0.83 ± 0.13	0.98 ± 0.15	0.26 ± 0.06	0.26 ± 0.07	0.68 ± 0.11	1.04 ± 0.14
[S III] λ9069	1.48 ± 0.21	1.62 ± 0.23	0.60 ± 0.10	0.61 ± 0.11	1.45 ± 0.18	1.82 ± 0.20

Notes.
[a] L_{obs} is the observed luminosity.
[b] L_{int} is the reddening-corrected luminosity.

closer to the central ionizing stars, showing a high degree of ionization, while the ratios are lower at the outer regions, indicating a low degree of ionization. We note that the integrated [O III] λ5007/Hα ratio of N44 D1 (2.52) is much higher than those of N44 D2 (1.67) and N44 C (0.55), which indicates the hardness of radiation field in N44 D1. The [O III] λ5007/Hβ ratio is also higher in N44 D1, representing the effect of high effective temperature of the ionizing star of spectral type O5 V. N44 D1, N44 D2, and N44 C show an [O III] λ5007/Hβ ratio of 7.89, 5.18, and 2.07, respectively. In N44 C, the high values of [O III] λ5007/Hα (~1.0–0.3) and [O III] λ5007/Hβ (~3.0—1.0) are near the O5 III star, and the values decrease toward the edge of the bubble.

5. Hα and Hβ Emission

5.1. Extinction Correction

The line luminosities are corrected for extinction using the intensity ratios $(H\alpha/H\beta)_{obs}$. Since the Hα/Hβ ratio is relatively sensitive to temperature, it can be used as a reliable reddening indicator. This ratio is compared with the theoretically expected value of the Balmer decrement $(H\alpha/H\beta)_{exp}$ for case B recombination (Osterbrock & Ferland 2006). Any deviation from the expected value of the Hα/Hβ ratio for a particular electron temperature can be associated with extinction. We estimate the nebular emission-line color excess $E(B-V)$ from the Hα/Hβ ratio using the equation from Domínguez et al. (2013),

$$E(B-V) = \frac{2.5}{k(\lambda_{H\beta}) - k(\lambda_{H\alpha})} \log_{10}\left[\frac{(H\alpha/H\beta)_{obs}}{(H\alpha/H\beta)_{exp}}\right]. \quad (1)$$

The expected value of the $(H\alpha/H\beta)_{exp}$ flux ratio is ~2.86 (Osterbrock & Ferland 2006). This value is obtained by assuming case B recombination at an electron temperature of 10,000 K and a density of 100 cm^{-3}. Then, following the extinction curve estimated by Calzetti et al. (2000),

$$k(\lambda) = 2.659(-1.857 + 1.040/\lambda) + R_V \quad (2)$$

for $\lambda = 0.63-2.2$ μm and

$$k(\lambda) = 2.659(-2.156 + 1.509/\lambda - 0.198/\lambda^2 + 0.011/\lambda^3) + R_V \quad (3)$$

for $\lambda = 0.12-0.63$ μm.

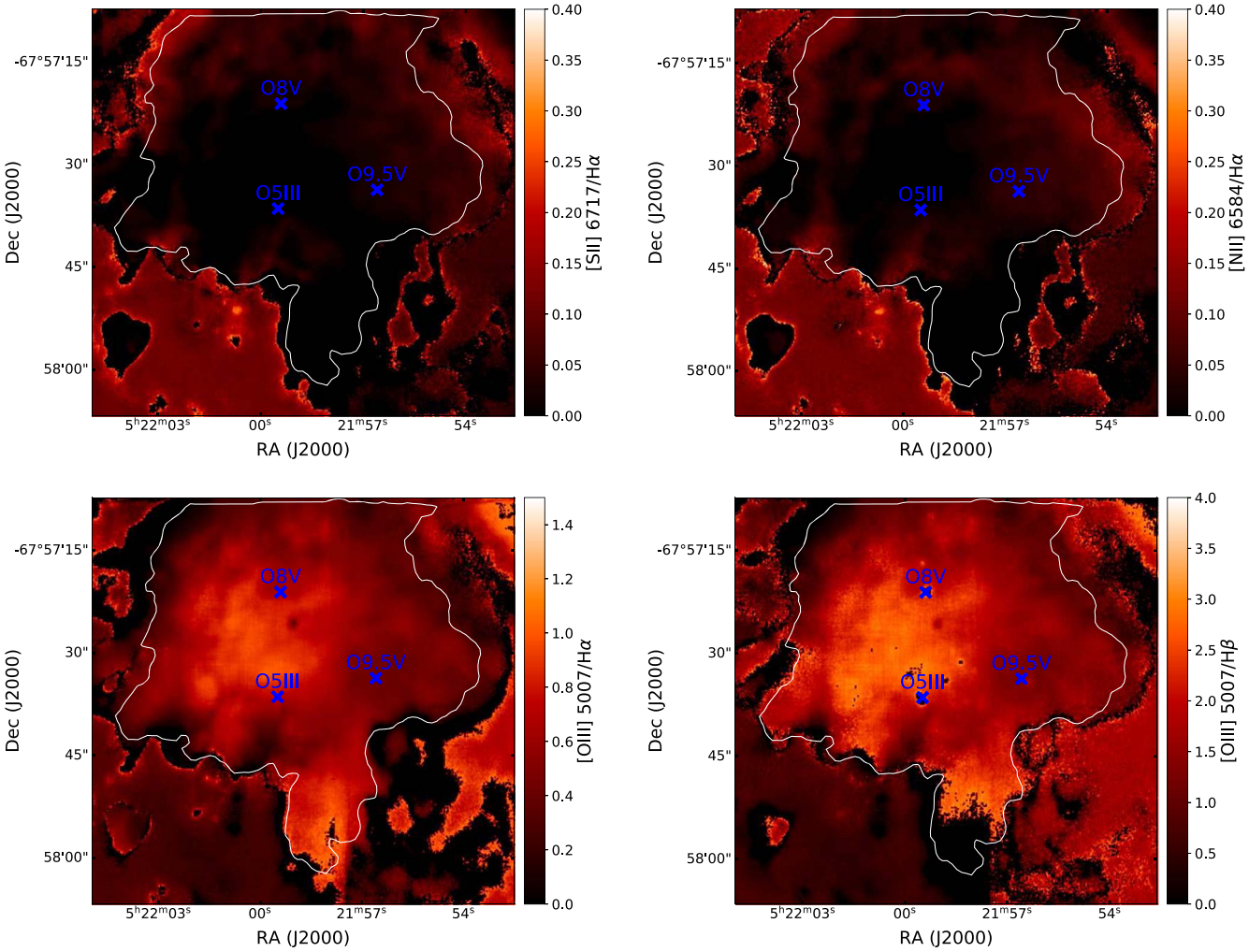

Figure 5. [S II] λ6717/Hα, [N II] λ6584/Hα, [O III] λ5007/Hα, and [O III] λ5007/Hβ ratio maps of the N44 C region. The white polygons represent the regions taken for analysis in this work, and blue crosses are the locations of hot stars.

Here $k(\lambda_{\mathrm{H}\alpha})$ and $k(\lambda_{\mathrm{H}\beta})$ are the extinction curves at Hα and Hβ wavelengths, respectively.

Assuming the ratio of total to selective extinction $R_V(=A_V/E(B-V))=3.1$, which is valid at optical wavelength for the LMC (Gordon et al. 2003), we get $k(\lambda_{\mathrm{H}\alpha})=2.38$ and $k(\lambda_{\mathrm{H}\beta})=3.65$.

Using the color excess $E(B-V)$, the extinction in magnitude is obtained by

$$A_{\mathrm{H}\alpha} = k(\lambda_{\mathrm{H}\alpha})E(B-V) \quad (4)$$

for the Hα line and

$$A_{\mathrm{H}\beta} = k(\lambda_{\mathrm{H}\beta})E(B-V) \quad (5)$$

for the Hβ line. Then, extinction-corrected Hα luminosity, L(Hα), is

$$L(\mathrm{H}\alpha) = L(\mathrm{H}\alpha)_{\mathrm{obs}}10^{0.4A_{\mathrm{H}\alpha}}, \quad (6)$$

and the extinction-corrected Hβ luminosity, L(Hβ), is

$$L(\mathrm{H}\beta) = L(\mathrm{H}\beta)_{\mathrm{obs}}10^{0.4A_{\mathrm{H}\beta}}. \quad (7)$$

Here $L(\mathrm{H}\alpha)_{\mathrm{obs}}$ and $L(\mathrm{H}\beta)_{\mathrm{obs}}$ are the observed luminosities of Hα and Hβ emission, respectively.

The values of the color excess $E(B-V)$ are 0.08 for N44 D1 and N44 D2 and 0.20 for N44 C. The extinction toward N44 D1 is $A_V=0.25$ mag. Our value agrees with the calculations by Garnett et al. (2000) and Lopez et al. (2014) for N44. N44 C has a significantly higher extinction, $A_V=0.62$ mag.

We applied the same method of extinction correction to other line emission, and the extinction-corrected luminosities (erg s^{-1}) are given in Table 2.

5.2. Lyman Continuum Photon Flux

The O-type stars in H II regions are the prominent sources of Lyman continuum photons. These stars deposit a bulk of their high-energy photons into the surrounding H II region within the Stromgren radii. If the gas is optically thick in the Lyman continuum, we expect all the ionizing photons emitted by the star to be absorbed. However, a significant fraction of these photons can escape on a larger scale outside of the H II region into the ISM. This fraction of photon leakage from H II regions needs to be measured to understand the overall energy budget and to probe whether the dominant hot stars in the region are responsible for the photoionization in the surrounding medium. We calculate the number of Lyman continuum photons (Q) absorbed in the region surrounding a hot star corresponding to Hα luminosities by assuming the case B recombination for electron temperature $T_e=10{,}000$ K and density $n_e=100$ cm^{-3}. The number of Lyman continuum photons related to Hα luminosity is obtained

Table 3
Emission-line Properties

Regions	Q (s^{-1})	Q_o (s^{-1})	f_{esc}	$\langle n_e \rangle$[a] (cm^{-3})	n_e [S II][b] (cm^{-3})	n_e [S II][c] (cm^{-3})
N44 D1	1.07×10^{49}	1.66×10^{49}	0.36	31	132 ± 50	141 ± 43
N44 D2	0.36×10^{49}	1.26×10^{49}	0.71	26	115 ± 45	121 ± 37
N44 C	1.02×10^{49}	3.37×10^{49}	0.70	38	66 ± 40	92 ± 35

Notes.
[a] $\langle n_e \rangle$ is the average electron density from Hα emission.
[b] n_e[S II] is the electron density derived using PYNEB.
[c] n_e[S II] is the electron density derived from Equation (11).

by $Q(\mathrm{H}\alpha) = 7.31 \times 10^{11} L(\mathrm{H}\alpha)$ photons s^{-1} (Kennicutt 1998; Osterbrock & Ferland 2006).

The numbers of ionizing photons derived from the Hα luminosity (Q) for N44 D1, N44 D2, and N44 C are tabulated in Table 3. To calculate the photon escape fraction, we also need to know the number of total Lyman continuum photons emitted by the ionizing stars. We adopt the model calculations (Q_0) for hot stars of appropriate spectral types from Martins et al. (2005). The Q_0 values of the only O5 V star in N44 D1; a combination of three ionizing stars of spectral types O5 III, O8 V, and O9.5 V in N44 C; and the O5.5 V star in N44 D2 are given in Table 3.

Using the Q and Q_0 values, we calculate the photon escape fraction,

$$f_{esc} = \frac{Q_0 - Q}{Q_0}. \quad (8)$$

McLeod et al. (2019) reported $f_{esc} \sim 0.37$ and 0.68 for N44 D1 and N44 C, respectively, using this method. We verify their determination and find that f_{esc} for N44 D1, N44 D2, and N44 C are 0.36, 0.71, and 0.70, respectively. These values imply that about 36% of the ionizing photons escape from N44 D1, 71% from N44 D2, and 70% from N44 C. N44 C shows a larger amount of photon leakage than N44 D1 and is more optically thin to the ionizing photon. This observation is consistent with the study of H II regions in the LMC by Pellegrini et al. (2012) that boundaries of optically thick regions are generally characterized by stratification in the ionization structures. The ionization structure of N44 D1 shows a well-defined nebular boundary where [O I] emission and [S II] emission peak at the outer boundary of the Hα emission and [O III] emission. The [S II]/Hα ratio map clearly shows the transition region in the ionization structure. N44 C does not show such an ionization stratification, while a slightly extended shell structure is found in the [S II]/Hα map.

Using the number of ionizing photons Q, we can also estimate the average electron density of emitting gas in an H II region, $\langle n_e \rangle$. Assuming the spherical nebula where H is fully ionized, the recombination balance equation is

$$Q = \frac{4\pi}{3} \alpha_B n_e^2 R_{\mathrm{H\,II}}^3. \quad (9)$$

Here α_B is the case B recombination coefficient $\sim 2.59 \times 10^{-13}$ cm^3 s^{-1} for gas at $T = 10{,}000$ K. $R_{\mathrm{H\,II}}$ is the mean radius of the H II region. Then, the average electron density from Hα emission is obtained by

$$\langle n_e \rangle = 177 \sqrt{\frac{Q_{48}}{R_{\mathrm{H\,II}}^3}}. \quad (10)$$

Here $Q_{48}(=Q/10^{48})$ is the number of Lyman continuum photons derived from the Hα luminosity and $R_{\mathrm{H\,II}}$ is the radius in parsecs. The $\langle n_e \rangle$ derived from Hα emission of N44 D1, N44 D2, and N44 C are 31, 26, and 38 cm^{-3}, respectively.

5.3. Electron Density

Electron density (n_e) and electron temperature (T_e) are two important physical parameters for characterizing an H II region. The n_e can be determined from the observed line intensities of two different energy levels with nearly equal excitation energy of the same ion. Their line ratios are generally not sensitive to T_e. The forbidden line ratio, [S II] $\lambda 6717/\lambda 6732$, is usually used to determine n_e, where [S II] $\lambda\lambda 6717$ and 6732 emission is relatively strong in the ionized nebula. Their corresponding critical density is $\sim 10^3$ cm^{-3}, hence probing the low-density regimes. McLeod et al. (2019) have reported $n_e \sim 152 \pm 42$ cm^{-3} for N44 C and $\sim 143 \pm 42$ cm^{-3} for N44 D1, applying the analytical solution given in McCall (1984) and assuming a T_e of 10,000 K. Toribio San Cipriano et al. (2017) have derived $n_e \sim 200 \pm 150$ cm^{-3} for a 3.0×9.4 $arcsec^2$ region closer to the ionizing star in N44 D1 using the [S II] $\lambda 6717/\lambda 6732$ ratio obtained from the VLT-UVES spectrum. Lopez et al. (2014) have reported a relatively low value of $n_e \sim 60$ cm^{-3} for the entire N44 using the flux density of the free–free emission at 3.5 cm. Garnett et al. (2000) derived $n_e < 160$ cm^{-3} for N44D1 using the [S II] $\lambda 6717/\lambda 6732$ ratio obtained with the 0.9 m telescope at Cerro Tololo Inter-American Observatory. McLeod et al. (2019) emphasize that densities derived from radio emission by Lopez et al. (2014) are expected to be smaller than those derived from the ratio of collisionally excited lines (Peimbert et al. 2017). These studies show a discrepancy in derived values of n_e for N44 D1 and N44 C; hence, we calculate the electron densities using [S II] $\lambda 6717/\lambda 6732$ ratios of N44 D1 and N44 C derived in our analysis of MUSE spectra. Electron temperature can be obtained by the forbidden line ratios [S III] $\lambda 6312/\lambda 9069$ and [N II] $\lambda 5755/\lambda 6384$; however, the MUSE observations of N44 D1 and N44 C show very weak [S III] $\lambda 6312$ and [N II] $\lambda 5755$ emission, which cannot be extracted from the data cube within a 5σ detection threshold in most of the pixels inside the defined polygons. We calculate the electron density as in McLeod et al. (2015) by applying the analytical solution in

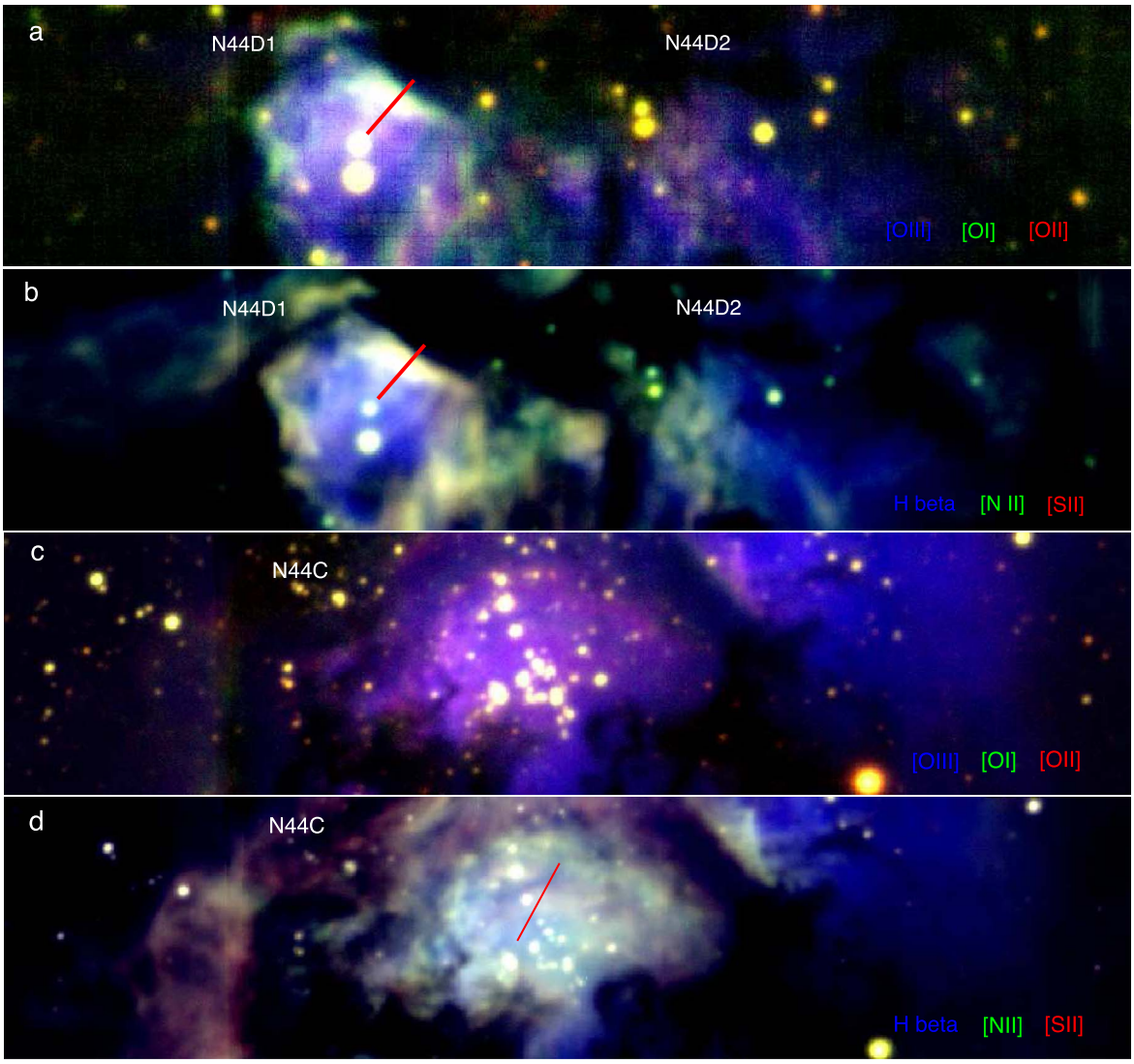

Figure 6. (a) Spatial distributions of N44 D1 and N44 D2 are shown in [O III] λ5007 (blue), [O II] λ7318 (red), and [O I] λ6300 emission (green). (b) N44 D1 and N44 D2 are shown in Hβ (blue), [S II] λ6717 (red), and [N II] λ6584 emission (green). (c) N44 C is shown in [O III] λ5007 (blue), [O II] λ7318 (red), and [O I] λ6300 emission (green). (d) N44 C is shown in Hβ (blue), [S II] λ6717 (red), and [N II] λ6584 emission (green). The ionization zone is traced by [O III] and Hβ, the partially ionized zone is traced by [O II] and [N II], and the ionization front is traced by [O I] λ6300 and [S II] λ6717. The observed spatial profiles in Figures 7 and 8 are taken along the crosscuts indicated as red lines in these maps.

McCall (1984),

$$n_e = \frac{1.49 - R_{\rm S\,II}}{12.8 \times R_{\rm S\,II} - 5.6713} \times 10^4 \ \ {\rm cm}^{-3}. \qquad (11)$$

Here $R_{\rm S\,II}$ is the [S II] λ6717/λ6732 ratio, and electron temperature is assumed to be 10,000 K as in McLeod et al. (2019). The derived n_e for N44D1, N44D2, and N44C using this method are 141 ± 43 cm^{-3}, 121 ± 37 cm^{-3}, and 92 ± 35 cm^{-3}, respectively. We also estimate n_e using the publicly available Python-based package PYNEB (Luridiana et al. 2013) for a comparison. This algorithm includes FIVEL (De Robertis et al. 1987) and NEBULAR (Shaw & Dufour 1995) packages for analyzing nebular emission lines. The package calculates the physical conditions (T_e and n_e) for a given set of emission-line intensities and returns the diagnostic plots. We use the density-sensitive [S II] λ6732/λ6717 line ratio to determine n_e using the diags.getTemDen task in PYNEB for a given T_e of 10,000 K. The estimated electron densities from PYNEB for N44D1, N44D2, and N44C are 132 ± 50 cm^{-3}, 115 ± 45 cm^{-3}, and 66 ± 40 cm^{-3}, respectively (Table 3). These density values are comparable to the density derived from Equation (11) within the estimated uncertainties.

6. Structure of Ionized Gas

To investigate the structure of ionization zones in N44 D and N44 C, we compare the spatial distribution of Hβ, [O III], [O II], [O I], [N II], and [S II] emission-line maps (Figure 6). The spatial distribution of [O III], [O II], and [O I] of N44 D1 in Figure 6(a) shows a clear stratification from ionization zones where [O III] λ5007 emission peaks around the O5 V star to the [O I] λ6300 emission at the ionization front. O'Dell & Wen (1992) have reported that [O I] λ6300 emission arises at the ionization front behind the PDR, between the ionization zone and molecular cloud. The majority of the [O I] λ6300 emission in H II regions is due to the collisional excitation by thermal electrons and atomic hydrogen via the charge exchange; hence, the intensity of [O I] λ6300 emission can be a measure of

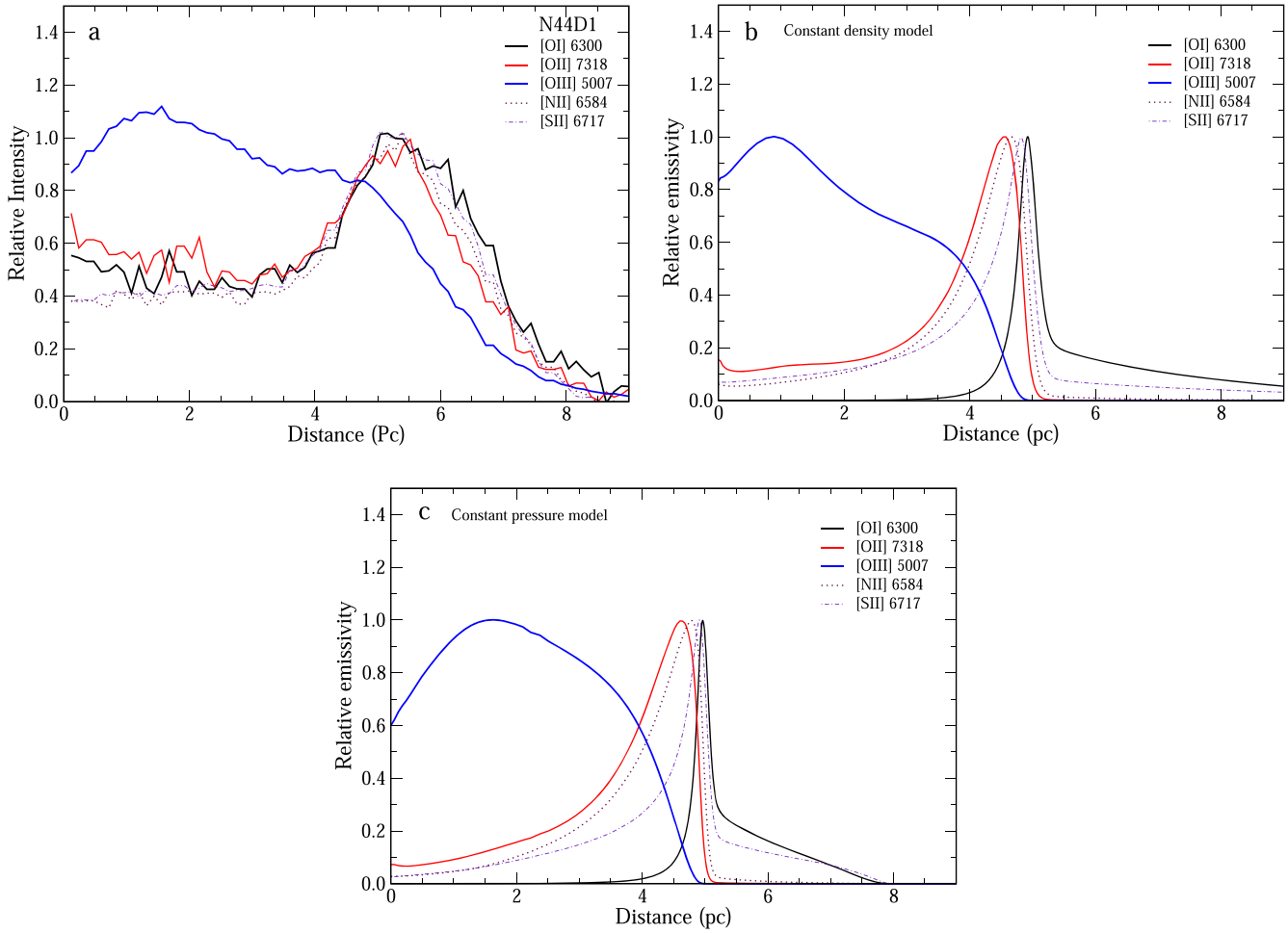

Figure 7. The spatial profiles of various emission lines in MUSE observations of N44 D1 are shown for comparison with the constant-density model and constant-pressure model. (a) The observed spatial profiles of [O I] λ6300, [O II] λ7318, [O III] λ5007, [N II] λ6584, and [S II] λ6717 emission of N44 D1 obtained by taking a crosscut (red line) shown in Figure 6. (b) The emission-line profiles of [O I] λ6300, [O II] λ7318, [O III] λ5007, [N II] λ6584, and [S II] λ6717 emission from the constant-density model of N44 D1 are shown for comparison. (c) The spatial profiles of [O I] λ6300, [O II] λ7318, [O III] λ5007, [N II] λ6584, and [S II] λ6717 emission from the constant-pressure model of N44 D1 are shown for comparison. The best-fit model line ratios for these models are given in Table 4. All the line emissivities are normalized to 1.0.

neutral hydrogen content. [O I] λ6300 in PDRs can also be collisionally excited by electrons ejected by dust grains and polycyclic aromatic hydrocarbons (PAHs) that absorb far-UV radiation emitted by the massive stars. In Figure 6(b), we compare the spatial distribution of Hβ (blue) and [N II] λ6584 (red) with [S II] λ6717 (green). [S II] emission is expected to peak at the ionization front. [N II] emission is found to be cospatial with [O II] emission that peaks at the partial ionization zone and concentrated in the outer boundary of the Hβ and [O III] emission. The structure of N44 D1 is nearly spherical, with only one important source of ionizing photons.

In Figure 7 we show the spatial profiles of various nebular emission lines by taking a crosscut along the northwestern edge of N44 D1. [O II] and [N II] emission is in a thin layer at the partial ionization zone outside [O III], but slightly interior to the [O I] emission. The [O I] emission is concentrated in a thin zone $\sim$4–7 pc located in the outer boundary of the H II region. Hα, Hβ, [O III], and He I are found to be cospatial in the ionization zone. In the outer layer of the ionization front in this H II region, we expect a well-defined PDR with a layer of C II, then H_2 emission, and a molecular cloud. High spatial resolution spectroscopic observations in infrared and submillimeter wavelengths are required for further studies of PDR properties. A similar ionization structure is reported in the Orion Nebula H II region. The [O I] λ6300 and [S II] λ6717 emission appears to peak along a bright bar at the ionization front in the outer boundary, which forms a thin transition layer of thickness $\sim 10^{15}$–10^{16} cm between the ionization zone and PDR. The emission from higher ionization species [O III] arises away from the ionization front and close to the ionizing star θ_1 Ori C (O'Dell et al. 2017; O'Dell 2001; Hester 1991; O'Dell & Wen 1992).

In N44 C, the [O III] λ5007 and Hβ emission appears to peak in the interior of the bubble near the ionizing star O5 III (Figures 6(c) and (d)). We show the spatial profiles of [O III], [O II], [S II], [N II], and Hα emission in N44 C, taking a crosscut from the position centroid of three ionizing stars to the northeast of N44 C (Figure 7). The spatial distributions of [O III] λ5007 and Hβ are similar and cospatial in the fully ionized zone. [O I] λ6300, [O II] λ7318, [N II] λ6584, and [S II] λ6717 emission does not form a well-defined outer boundary but appears as patches of emission bars within the [O III] λ5007 and Hβ emission region.

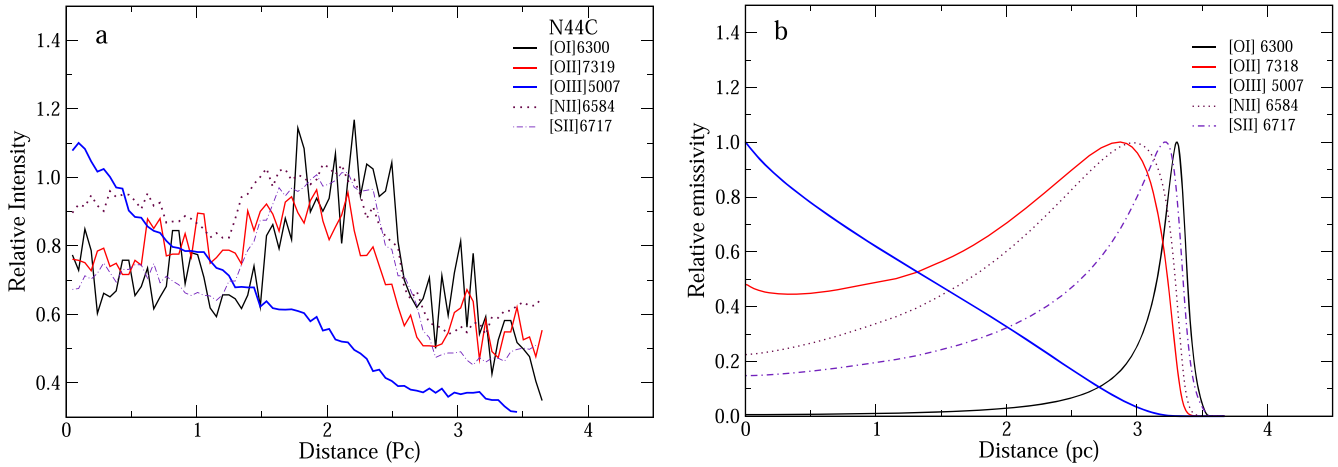

Figure 8. (a) The observed spatial profiles of [O I] λ6300, [O II] λ7318, [O III] λ5007, [N II] λ6584, and [S II] λ6717 emission of N44 C obtained by taking a crosscut (red line) shown in Figure 6. (b) The spatial profiles of [O I] λ6300, [O II] λ7318, [O III] λ5007, [N II] λ6584, and [S II] λ6717 emission from the constant-density model obtained for N44 C are shown for comparison. The best-fit model line ratios for this model are given in Table 5.

7. Comparison with Photoionization Model

The MUSE observations of N44 in the LMC show that the two bright H II regions N44 D1 and N44 C have different ionization geometries and physical characteristics. N44 D1 has Hα and Hβ surface brightness values 0.03 dex and 0.1 dex higher than N44 C. [O III]/Hβ and [O III]/Hα ratios in N44 D1 are considerably larger than in N44 C, indicating a higher degree of ionization. N44 D1 shows a higher [O I] λ6300/Hβ ratio with a well-defined [O I] λ6300 emission at the H II region outer boundary, indicating an ionization front.

In the ideal case, the [O I] λ6300 emission dominates at the outer boundary of the H II region, where the neutral hydrogen density dominates; hence, we expect most of the Lyman continuum photons are absorbed by the nebula, and are ionization bounded. This is an optically thick case, where we find a shell of [O I] λ6300 emission at the ionization front, indicating the border of the H II region. In the density-bounded H II regions, there is no well-defined ionization front surrounding highly ionized gas, and most of the Lyman continuum photons leak from the cloud contributing to the diffuse ionized gas outside of the cloud. In such cases, there is a weak [O I] λ6300 emission condensation within the H II region or no shell structure at the boundary. In a blister H II region, there is a partial ionization front at the boundary, which does not cover the nebula completely; hence, the photons escape in certain directions. Our study of the [O I] λ6300 emission in N44 D1 and N44 C reveals these different observational properties of H II regions. Moreover, the measurement of the photon leakage using the Hα emission indicates that N44 D1 and N44 C have photon escape fractions of 36% and 70%, respectively. These calculations are in agreement with the study of the photon leakage by McLeod et al. (2019). The remaining ionizing photons are trapped within the H II region itself and affect the overall ionization balance. Pellegrini et al. (2011, 2012) reported that the ionization-bounded H II regions are constrained to an escape fraction $<$0.6 and those with density-bounded regions are $>$0.6.

To further interpret these observations, we compute various photoionization models for comparing the emission-line ratios and the geometry of ionization structure. We model the ionization structure of N44 D1 and N44 C using the photoionization code CLOUDY (Ferland et al. 2017). We derive the emissivities of prominent ionic species across the H II region, from the illuminated face of the H^+ region through the partially ionized zone to the neutral ionization front, where ionizing radiation has been attenuated and becoming neutral to the molecular zone. We develop various photoionization models for N44 D1 and N44 C, and we test which model can better match the observed ionization geometry of the cloud and emission-line ratios. To compare the ionization geometry, we use the spatial profiles of the line emissions along the H II regions (Figures 7 and 8). The emission-line ratios we use for tests are given in Tables 4 and 5. The [S II] λ6717/λ6732 line ratio is sensitive to electron density, and [O II] (λ7318+λ7329)/[O III] λ5007 to the ionization parameter. [O III] λ5007/Hα, [O III] λ5007/Hβ, [O II]/Hβ, [N II]/Hβ, and [O I]/Hβ give the behavior of different ionization zones and are also sensitive to the metallicity. These line ratios are very sensitive to the adopted input parameters. A built-in optimization program based on the PHYMIR algorithm (van Hoof 1997; van Hoof et al. 2013; Ferland et al. 2013) is used to obtain the best-fit model, which applies a χ^2 minimization to determine the goodness of fit by varying the input parameters. We vary the total hydrogen density (*hden*), Φ(H), *brems*, and filling factor to find the best agreement between the model with the observed line ratios and geometry. Sometimes, for a given set of constraints, some observables are optimized very well compared to the other sets, and the best-fit model is obtained by the overall χ^2. Therefore, we manually fine-tuned certain parameters until the best-matching line ratios with the observations are obtained. Finally, the model line ratios are compared with the observed line ratios, and the best-fit model was determined by calculating the χ^2 as (Mondal et al. 2017; Pavana et al. 2019)

$$\chi^2 = \sum_{i=1}^{n} (M_i - O_i)^2/\sigma_i^2. \quad (12)$$

Here, the number of observed lines is n, M_i is the model line ratio, O_i is the observed line ratio, and σ_i is the error in the observed flux ratio. The best optimized model line ratios, observed line ratios, and χ^2 values are given in Tables 4 and 5.

The basic input parameters to CLOUDY require the geometry of the cloud, intensity of incident ionizing photon flux, elemental abundances, and gas density.

Table 4
Model Line Ratios Compared with Observations for N44 D1

Line Ratios	Observed ratios	Pressure Model $\Phi(H)_{10.15}$	χ^2	Density Model $\Phi(H)_{10.14}$	χ^2
[S II] λ6717/λ6732	1.32 ± 0.40	1.28	0.01	1.32	0.00
[O II] (λ7318+λ7329)/[O III] λ5007	0.008 ± 0.002	0.004	4.0	0.006	1.00
[O III] λ4959/λ5007	0.33 ± 0.07	0.33	0.00	0.33	0.00
[O III] λ5007/Hβ	7.89 ± 1.60	6.76	0.50	7.10	0.24
[S III] λ9069/Hβ	0.31 ± 0.08	0.36	0.40	0.37	0.56
[O II] λ7329/Hβ	0.03 ± 0.01	0.02	1.0	0.02	1.00
[S II] λ6717/Hβ	0.24 ± 0.10	0.36	1.44	0.34	1.00
[N II] λ6584/Hβ	0.17 ± 0.05	0.14	0.36	0.14	0.36
[O I] λ6300/Hβ	0.07 ± 0.05	0.15	2.56	0.14	1.96
[O III] λ5007/Hα	2.52 ± 0.50	2.40	0.06	2.51	0.00
[S II] λ6717/Hα	0.08 ± 0.02	0.13	6.30	0.12	4.00
[N II] λ6584/Hα	0.05 ± 0.02	0.05	0.00	0.05	0.00
T_e over radius (K)		12,491		12,410	
n_e over radius (cm^{-3})		175		136	

7.1. Geometry

Observations show a clear ionization stratification in N44 D1. The ionized gas is traced by [O III] λ5007 and Hβ emission, and the ionization front is traced by [O I] λ6300 and [S II] λ6717 emission. The line ratio maps show a nearly radial symmetry around the ionizing star. This structure is quite simple to model, as observation shows that there is only a prominent source of the ionizing photon at the cloud's interior. For N44 D1, we calculate an optically thick spherical model with a covering factor 0.64. We choose an outer radius $R = 7.4$ pc based on the observed geometry (Figure 7). McLeod et al. (2019) report a radius containing 90% of the Hα emission, $R_{90} = 7.4$ pc for N44 D1, which agrees with the adopted radius in our model. The model constitutes the exciting star at the center of a spherical cloud, surrounded by the layers of the H II region and PDR.

MUSE observation of N44 C does not show a clear ionization stratification as in N44 D1. However, observations indicate that the majority of photons escape from N44 C and the region harbors three ionizing stars (see Figure 1). Therefore, we adopt an optically thin open geometry for N44 C with a covering factor 0.3 and a radius of $R = 6.93$ pc.

7.2. Stellar Continuum

We use OSTAR TLUSTY models in CLOUDY for defining the stellar continuum. We choose a model with an effective temperature ($T_{\rm eff}$) of 41,540 K, gravity (log$g$) of 3.92, and metallicity of 0.5 $Z_\odot$, which is appropriate for a spectral class O5 V star (McLeod et al. 2019) in N44 D1. The radiation field from this O5 V star corresponds to an incident flux of ionizing photons, $\log \Phi(H) = 9.98$ photons s^{-1} cm^{-2} at the ionization front of N44 D1 traced by the peak of [O I] λ6300 emission. Here $\Phi(H) = Q(H)/4\pi r^2$, where the number of ionizing photons per second Q(H) is 1.82×10^{49} photons s^{-1}, and r is the distance from the ionizing star to the cloud illumination face. We note that the flux of ionizing photons Φ(H) plays a significant role in the shape of spatial profiles and lines strengths; hence, we test the models with varying Φ(H) until the best-fit model is obtained. For N44 D1 we vary the Φ(H) in a range 9.98−10.60 photons s^{-1} cm^{-2}.

Observations show that N44 C encloses three hot stars of spectral types O5 III, O8 V, and O9.5 V; hence, we chose three hot star model atmospheres from TLUSTY. We adopt models with $T_{\rm eff} = 39{,}500$ K and log$g = 3.69$ for spectral type O5 III, $T_{\rm eff} = 33{,}400$ K and log$g = 3.92$ for an O8 V star, and $T_{\rm eff} = 30{,}500$ K and log$g = 3.92$ for an O9.5 V star with a metallicity of 0.5 $Z_\odot$.

Table 5
Model Line Ratios Compared with Observations for N44 C

Line Ratios	Observed ratios	Model ratios	χ^2
[S II] λ6717/λ6732	1.37 ± 0.4	1.35	0.002
[O II] (λ7318+λ7329)/ [O III] λ5007	0.04 ± 0.02	0.02	1.00
[O III] λ4959/λ5007	0.34 ± 0.01	0.33	1.00
[O III] λ5007/Hβ	2.07 ± 0.6	1.75	0.28
[S III] λ9069/Hβ	0.39 ± 0.1	0.28	1.20
[O II] λ7329/Hβ	0.03 ± 0.02	0.02	0.25
[S II] λ6717/Hβ	0.25 ± 0.08	0.30	0.39
[N II] λ6584/Hβ	0.26 ± 0.08	0.19	0.76
[O I] λ6300/Hβ	0.03 ± 0.01	0.03	0.00
[O III] λ5007/Hα	0.55 ± 0.14	0.63	0.32
[S II] λ6717/Hα	0.07 ± 0.02	0.10	2.25
[N II] λ6584/Hα	0.07 ± 0.02	0.07	0.00
T_e over radius (K)		10 709	
n_e over radius (cm^{-3})		84	

We expect the X-rays to significantly affect the ionization balance of the gas, since the observed total X-ray luminosity is in a comparable range to that of the observed Hα luminosity in both N44 D1 and N44 C. Chu et al. (1993) have presented the global X-ray emission in N44 using observations with the ROSAT satellite. They reported a diffuse X-ray luminosity of $(0.29-3.5) \times 10^{37}$ erg s^{-1} at a characteristic temperature $(1.6-2.5) \times 10^6$ K. We vary the bremsstrahlung temperature (*brems*) in a range $(1.6-2.5) \times 10^6$ K.

7.3. Abundances

We follow the abundances provided by Toribio San Cipriano et al. (2017) for C and O and Garnett et al. (2000) for He, N, Ne, S, and Ar. For the remaining species, we use the standard values included in CLOUDY for H II regions (Baldwin et al. 1991) and adopt an overall gaseous metallicity of 0.5 $Z_\odot$. Since

the dust contributes significantly to heating and the overall equilibrium of the photoionized gas in the cloud, we also include the dust grains with a metallicity scaled to half solar.

7.4. Density

For gas density at the illuminated face of the cloud, we use the range of electron density values obtained from the Hα luminosity and [S II] $\lambda6717/\lambda6732$ line ratio ($30\ \mathrm{cm}^{-3} \leqslant n_e \leqslant 180\ \mathrm{cm}^{-3}$) for N44 D1. For N44 C, we varied the density between 40 and $100\,\mathrm{cm}^{-3}$ and finally obtained a value consistent with the observed electron density obtained from the [S II] $\lambda6717/\lambda6732$ ratio ($66\,\mathrm{cm}^{-3}$). We compute models with constant density and constant pressure in a time-steady hydrostatic cloud. When we use a filling factor of 1, we find that most of the predicted line ratios differ from the observed values, and the ratios considerably change when we use a filling factor <1. We estimate an approximate range of filling factors using the relation $N^2{}_e(\mathrm{rms}) = \epsilon\, N_e^2(\mathrm{local})$ (Relano et al. 2002). Here N_e(rms) is taken as the average electron density derived from Hα flux and N_e(local) is the electron density obtained from the [S II] $\lambda6717/\lambda6732$ ratio.

We note that the total gas pressure and radiation pressure vary with the position and width of the ionization front. This can also be a result of varying density at the ionization front as pressure changes. If density increases, the ionization front pushes the interior to the cloud, increasing the line emissivities. We therefore tested two models: one with constant-pressure distribution and the other with constant-density distribution.

7.5. Constant-pressure and Constant-density Distribution

In the constant-pressure model, the total pressure is kept constant throughout the cloud. The sum of gas pressure, line radiation pressure, turbulent pressure, and the outward pressure of starlight remains constant. At any particular region on the cloud, the resulting forces are due to the various contributions to the pressure balance. Therefore, the cloud remains in hydrostatic equilibrium. The hydrostatic equilibrium model would balance the pressure gradient due to the kinetic energy and momentum carried by stellar photon flux, with the thermal gas pressure exerted by ionized gas. However, this model significantly changes the gas density and width of the ionization front. The constant density represents the total hydrogen density constant throughout the nebula, but electron and molecular fractions vary with depth. In Figure 8, we compare the spatial profiles of various emission lines, [O I] $\lambda6300$, [O II] $\lambda7318$, [O III] $\lambda5007$, [N II] $\lambda6584$, and [S II] $\lambda6717$, obtained for N44 D1 with constant-density and constant-pressure models. We note that constant-pressure models provide narrower ionization fronts than constant-density models. Pellegrini et al. (2007, 2009) applied constant-pressure models to the Orion bar and M17 PDRs for a self-consistent simulation of H^+, H^0, and H_2 regions, including additional turbulent pressure and magnetic field. In that model, the physical depth, the separation of H^0 and H_2, and overall geometry depend on the gas density. In our constant-pressure model, we include additional turbulence of $10\,\mathrm{km\,s}^{-1}$. This provides turbulent line broadening in addition to the thermal line broadening and slightly increases the widths of the spatial profiles in the ionization front. Pellegrini et al. (2007, 2009) found that the presence of a magnetic field significantly increases the physical width of the PDR, as a result of reduced gas density and increased photon path length. We calculate the constant-pressure models consisting of gas pressure and turbulent pressure. We did not include the pressure due to the magnetic field, as currently there is no observational evidence of a magnetic field in N44. In Table 4 we show the diagnostic line ratios obtained for both constant-pressure and constant-density models, along with the observed line ratios of N44 D1. We note that the constant-pressure model describes most of the line ratios; however, we obtain reduced χ^2 for most of the line ratios in the constant-density model. We also note that the geometry of the [O III] $\lambda5007$ spatial profile matches reasonably well with the observation in the constant-density model. The constant-pressure model predicts a relatively larger electron density than observed. Our studies show that the depth of the H^+ region, the width of the ionization front, and the overall geometry of the emission-line profiles with depth are largely dependent on the thermal gas pressure and stellar radiation pressure. Within H^+ regions, the density can be constant with the depth; hence, the predicted line ratios have a minimal effect on the chosen equation of state.

7.6. Photoionization Model of N44 D1

Even though observations give a photon escape fraction of 0.36 for N44 D1, it does not mean that the H II region is completely ionization bounded. We expect the photon leakage from some part of the cloud; hence, that direction can be density bounded, and the remaining part of the cloud can be ionization bounded. This model can be a blister-type H II region as suggested by Pellegrini et al. (2011). It is also interesting to note that N44 D1 shows relatively large [O III]/Hβ ratios, implying a large ionization parameter, which can be a result of the high effective temperature of the only ionizing (O5 V) star in N44 D1. However, to obtain a high [O III]/Hβ ratio, we include an additional contribution from a bremsstrahlung component with the temperature in a range $10^{6.2}$–$10^{6.4}$ K. This plasma temperature is inferred from the studies of the X-ray emission by Chu et al. (1993). These authors have reported an excess of X-ray emission in the N44 D region. This excess X-ray emission can be shock driven owing to massive stellar winds or the off-center supernova remnant. We find that partial ionization-bounded geometry with constant-density models can reproduce reasonably well the observed geometry and line ratios of N44 D1 for a $\log \Phi(\mathrm{H}) = 10.14$ photons $\mathrm{s}^{-1}\,\mathrm{cm}^{-2}$, electron density $136\,\mathrm{cm}^{-3}$, and bremsstrahlung temperature 1.67×10^6 K.

7.7. Photoionization Model of N44 C

The observed geometry of N44 C does not give a well-defined ionization front at the H II region boundary, and the patches of [S II] and [O II] concentrations are found closer to the cloud centroid. We obtain an optimal model for N44 C by applying an optically thin constant-density distribution. We note that the shape of the incident radiation mainly depends on three fixed stellar atmosphere models, which are appropriate for three enclosed hot stars O5 III, O8.5 V, and O9.5 V. The [O III]/Hβ ratio in N44 C is relatively low compared to N44 D1, indicating low ionization parameter, and to obtain this gas ionization, we did not include any additional bremsstrahlung component as in N44 D1. Since the observations show that 70% of photons escape from N44 C, we use an optically thin open geometry where the Lyman continuum optical depth

(τ_{912}) is found to be very low (<1); hence, the majority of the cloud is open to the Lyman photons. We note that this model can reasonably well describe the observed geometry and the line ratios of N44 C. Figure 8 shows the model emission-line profiles as a function of depth in the nebula, and the line ratios are given in Table 5. Comparison of our models with the observed geometry and line ratios indicates that N44 C has an optically thin geometry and the region is being energized mainly by the outward momentum carried by the radiation pressure from three ionizing stars.

8. Conclusions

We carry out a detailed analysis of two H II regions in N44 using the integral field optical spectroscopic observations obtained with MUSE. Comparing these observations with the photoionization models computed with CLOUDY, we describe the spatial distribution of emission-line geometry and the physical conditions. Our results are summarized as follows:

1. Our analysis reveals that the spatial distribution of various spectral lines in N44 D1 provides a stratified ionization geometry. The central ionizing star is covered by a fully ionized hydrogen gas, and at the periphery there is a well-defined transition zone from O^{++} through O^{+} to the neutral zone O^{0}. Hα, Hβ, and [O III] emission is cospatial and peaks at the fully ionized zone, while [O II], [N II], [S II], and [O I] emission peaks at the outer boundary. This region provides an excellent site for modeling an ideal H II region with a stratified ionization geometry. The [O I] λ6300 emission of the N44 D1 region reveals a clear boundary/transition zone in the outer boundary of [O III] λ5007 and [O II] λ7329 emission, which does not cover the entire nebula completely, indicating a partial ionization front. Comparing these studies with Pellegrini et al. (2011, 2012), we suggest that the N44 D1 is a blister H II region.
2. The spatial distributions of various spectral lines in N44 C do not show a stratified ionization front at the boundary. However, it shows the condensations of [S II] and [N II] emission within the H II region. The [O I] λ6300 emission is relatively weak in N44 C and does not show a well-defined outer boundary as in N44 D1. These observations support relatively higher photon escape fraction reported by McLeod et al. (2019), suggesting that N44 C is a density-bounded optically thin H II region.
3. Our studies reveal that the [O III]/Hα and [O III]/Hβ line ratios give a clear indication of a higher degree of ionization in the regions closer to the ionizing stars and the ratios are lower toward the boundary of N44 D1 and N44 C. [S II]/Hα and [N II]/Hβ line ratio maps show a shell structure in both N44 D1 and N44 C. [O III]/Hα and [O III]/Hβ of N44 D1 are much higher than N44 C, indicating a harder radiation field. The effective temperature of the hot star plays a key role here because N44 D1 has a hotter ionizing star (O5 V) than N44 C (O5 III).
4. We use our results of spatially resolved MUSE spectra to explore the photoionization models with CLOUDY that can well describe the observed geometry and emission-line ratios. We find that the constant-density model gives better geometry and line ratios than the constant-pressure model in N44 D1. An ionization-bounded geometry with a partial covering factor can well reproduce the observed geometry and line ratios, indicating that N44 D1 is a blister H II region. The spatial profile of [O III] λ5007 matches very nicely with the observation. Model calculations reveal that a significant amount of X-ray emission takes part in shaping the geometry of the emission-line profiles, in addition to the ionizing radiation from the O5 V star. The electron density and temperature values from this model are also consistent with our measurements from the observed values.
5. An optically thin and open geometry model has been applied to reproduce the observed geometry and line ratios in N44 C. The modeling results show that the N44 C region is mainly energized by the radiation from three ionizing stars. Our studies indicate that the ionization structure and physical conditions in N44 D1 and N44 C are set by the stellar radiation pressure and gas thermal pressure.

This research has been supported by the United Arab Emirates University (UAEU) through UAEU Program for Advanced Research (UPAR) grant G00003479 and start-up grant G00002964. This paper makes use of the following MUSE (VLT) data: program ID: 096.C-0137(A). F.K. acknowledges the Ministry of Science and Technology of Taiwan for the grant MOST107-2119-M-001-031-MY3 and Academia Sinica Investigator Award, AS-IA-106-M03. M.S. acknowledges the NASA award, 80GSFC21M0002 (M.S.). K.T. acknowledges Grants-in-Aid for Scientific Research (KAKENHI) of Japan Society for the Promotion of Science (JSPS; grant No. 21H00049).

ORCID iDs

Naslim Neelamkodan https://orcid.org/0000-0001-8901-7287
Suzanne C. Madden https://orcid.org/0000-0003-3229-2899
Marta Sewilo https://orcid.org/0000-0003-2248-6032
Francisca Kemper https://orcid.org/0000-0003-2743-8240
Kazuki Tokuda https://orcid.org/0000-0002-2062-1600
Toshikazu Onishi https://orcid.org/0000-0001-7826-3837

References

Allen, M. G., Groves, B. A., Dopita, M. A., Sutherland, R. S., & Kewley, L. J. 2008, ApJS, 178, 20
Baldwin, J. A., Ferland, G. J., Martin, P. G., et al. 1991, ApJ, 374, 580
Calzetti, D., Armus, L., Bohlin, R. C., et al. 2000, ApJ, 533, 682
Chu, Y.-H., Mac Low, M.-M., Garcia-Segura, G., Wakker, B., & Kennicutt, R. C. J. 1993, ApJ, 414, 213
De Robertis, M. M., Dufour, R. J., & Hunt, R. W. 1987, JRASC, 81, 195
Della Bruna, L., Adamo, A., Bik, A., et al. 2020, A&A, 635, A134
Domínguez, A., Siana, B., Henry, A. L., et al. 2013, ApJ, 763, 145
Ferland, G. J., Chatzikos, M., Guzmán, F., et al. 2017, RMxAA, 53, 385
Ferland, G. J., Porter, R. L., van Hoof, P. A. M., et al. 2013, RMxAA, 49, 137
García-Díaz, M. T., & Henney, W. J. 2007, AJ, 133, 952
Garnett, D. R., Galarza, V. C., & Chu, Y.-H. 2000, ApJ, 545, 251
Gordon, K. D., Clayton, G. C., Misselt, K. A., Landolt, A. U., & Wolff, M. J. 2003, ApJ, 594, 279
Hester, J. J. 1991, PASP, 103, 853
Kennicutt, R. C. J. 1998, ARA&A, 36, 189
Lopez, L. A., Krumholz, M. R., Bolatto, A. D., et al. 2014, ApJ, 795, 121
Lucke, P. B., & Hodge, P. W. 1970, AJ, 75, 171
Luridiana, V., Morisset, C., & Shaw, R. A. 2013, PyNeb: Analysis of Emission Lines, Astrophysics Source Code Library, ascl:1304.021
Martins, F., Schaerer, D., & Hillier, D. J. 2005, A&A, 436, 1049

McCall, M. L. 1984, MNRAS, 208, 253
McLeod, A. F., Dale, J. E., Evans, C. J., et al. 2019, MNRAS, 486, 5263
McLeod, A. F., Dale, J. E., Ginsburg, A., et al. 2015, MNRAS, 450, 1057
Mondal, A., Anupama, G. C., Kamath, U. S., et al. 2017, MNRAS, 474, 4211
Naslim, N., Kemper, F., Madden, S. C., et al. 2015, MNRAS, 446, 2490
Naslim, N., Tokuda, K., Onishi, T., et al. 2018, ApJ, 853, 175
Nayana, A. J., Naslim, N., Onishi, T., et al. 2020, ApJ, 902, 140
O'Dell, C. R. 2001, ARA&A, 39, 99
O'Dell, C. R., Kollatschny, W., & Ferland, G. J. 2017, ApJ, 837, 151
O'Dell, C. R., & Wen, Z. 1992, ApJ, 387, 229
Oey, M. S., & Massey, P. 1995, ApJ, 452, 210
Osterbrock, D. E., & Ferland, G. J. 2006, Astrophysics of Gaseous Nebulae and Active Galactic Nuclei (Singapore: University Science Books)
Pavana, M., Anche, R. M., Anupama, G. C., Ramaprakash, A. N., & Selvakumar, G. 2019, A&A, 622, A126
Peimbert, M., Peimbert, A., & Delgado-Inglada, G. 2017, PASP, 129, 082001
Peimbert, M., Peimbert, A., & Ruiz, M. T. 2000, ApJ, 541, 688
Pellegrini, E. W., Baldwin, J. A., Brogan, C. L., et al. 2007, ApJ, 658, 1119
Pellegrini, E. W., Baldwin, J. A., & Ferland, G. J. 2010, ApJS, 191, 160
Pellegrini, E. W., Baldwin, J. A., Ferland, G. J., Shaw, G., & Heathcote, S. 2009, ApJ, 693, 285
Pellegrini, E. W., Oey, M. S., Winkler, P. F., et al. 2012, ApJ, 755, 40
Pellegrini, E. W., Oey, M. S., Winkler, P. F., Smith, R. C., & Points, S. 2011, BSRSL, 80, 410
Pietrzyński, G., Graczyk, D., Gallenne, A., et al. 2019, Natur, 567, 200
Pogge, R. W., Owen, J. M., & Atwood, B. 1992, ApJ, 399, 147
Polles, F. L., Madden, S. C., Lebouteiller, V., et al. 2019, A&A, 622, A119
Relaño, M., Monreal-Ibero, A., Vílchez, J. M., & Kennicutt, R. C. 2010, MNRAS, 402, 1635
Relano, M., Peimbert, M., & Beckman, J. 2002, ApJ, 564, 704
Rosolowsky, E. W., Pineda, J. E., Kauffmann, J., & Goodman, A. A. 2008, ApJ, 679, 1338
Shaw, R. A., & Dufour, R. J. 1995, PASP, 107, 896
Smith, R. C. & MCELS Team 1998, PASA, 15, 163
Toribio San Cipriano, L., Domínguez-Guzmán, G., Esteban, C., et al. 2017, MNRAS, 467, 3759
van der Marel, R. P., & Cioni, M.-R. L. 2001, AJ, 122, 1807
van Hoof, P. A. M. 1997, PhD thesis, Utrecht Univ.
van Hoof, P. A. M., Van de Steene, G. C., Exter, K. M., et al. 2013, A&A, 560, A7
Westerlund, B. E. 1997, The Magellanic Clouds (Cambridge: Cambridge Univ. Press)